Cite as: B. E. Kelly *et al.*, *Science* 10.1126/science.aau7114 (2019).

Volumetric additive manufacturing via tomographic reconstruction

Brett E. Kelly[1,2]*, Indrasen Bhattacharya[3]*, Hossein Heidari[1]*, Maxim Shusteff[2], Christopher M. Spadaccini[4], Hayden K. Taylor[1]†

[1]Department of Mechanical Engineering, University of California, Berkeley, Berkeley, CA 94720, USA. [2]Materials Engineering Division, Lawrence Livermore National Laboratory, Livermore, CA 94550, USA. [3]Applied Science and Technology program, University of California, Berkeley, Berkeley, CA 94720, USA. [4]Engineering Directorate, Lawrence Livermore National Laboratory, Livermore, CA 94550, USA.

*These authors contributed equally to this work.

†Corresponding author. Email: hkt@berkeley.edu

Additive manufacturing promises enormous geometrical freedom and the potential to combine materials for complex functions. The speed, geometry, and surface quality limitations of additive processes are linked to the reliance on material layering. We demonstrated concurrent printing of all points within a three-dimensional object by illuminating a rotating volume of photosensitive material with a dynamically evolving light pattern. We print features as small as 0.3 mm in engineering acrylate polymers, as well as printing soft structures with exceptionally smooth surfaces into a gelatin methacrylate hydrogel. Our process enables us to construct components that encase other pre-existing solid objects, allowing for multi-material fabrication. We developed models to describe speed and spatial resolution capabilities. We also demonstrated printing times of 30–120 s for diverse centimeter-scale objects.

Additive manufacturing (AM) technologies are increasingly used to produce end-use, multi-component, and multi-material parts (*1*). They meet fabrication needs in applications including patient-specific medical devices (*2*, *3*), optics (*4*), microfluidics (*5*), aerospace components (*6*), fixturing (*7*), and tooling (*8*). Current AM processes create 3D geometries through repeated one- or two-dimensional unit operations (*9*–*12*). Such layer-by-layer approaches limit throughput, degrade surface quality, constrain geometric capabilities, increase post-processing requirements, and may cause anisotropy of mechanical performance. A manufacturing technique capable of simultaneously fabricating all points within an arbitrary three-dimensional geometry would provide a different strategy to address these issues and complement existing AM methods. A method that forms parts volumetrically allows for different ways to integrate multiple components and may widen the material landscape to enhance the functionality of finished parts (*1*).

We developed a method, Computed Axial Lithography (CAL), that allowed us to synthesize arbitrary geometries volumetrically through photopolymerization. The CAL approach has several advantages over conventional layer-based printing methods. The method may be used to circumvent support structures as it can print into high viscosity fluids or even solids. Printing 3D structures around preexisting solid components is also possible with our approach. CAL is scalable to larger print volumes, and is several orders of magnitude faster, under a wider range of conditions, than layer-by-layer methods.

The CAL manufacturing system we developed selectively solidifies a photosensitive liquid within a contained volume. We delivered light energy to the material volume as a set of two-dimensional images. Each image projection propagates through the material from a different angle. The superposition of exposures from multiple angles (Fig. 1A) results in a three-dimensional energy dose sufficient to solidify the material in the desired geometry. Our process was inspired by the image reconstruction procedures of Computed Tomography (CT), a technique that finds wide use in medical imaging and non-destructive testing (*13*, *14*). The core concepts of CT can be directly applied to additive fabrication. A related dose delivery method is intensity modulated radiation therapy (IMRT) for cancer treatment (*15*). IMRT creates a 3D exposure inside a patient's body to target tumor regions with a critical radiation dose, while limiting the dose in regions containing vital organs. The CAL process is able to recover exactly the sculpted geometry (fig. S7) as the response of the material to the optical dose is nonlinear, unlike in IMRT.

We designed a physical system in order to fabricate 3D parts (Fig. 1B). We used a digital video projector to output our computed intensity-modulated projections, which we time-sequenced to the rotation rate of the uncured photopolymer precursor material. Free radicals are generated by light activation and then rapidly quenched and deactivated by oxygen

Downloaded from http://science.sciencemag.org/ on January 31, 2019

during the initial, inhibition phase of printing (*16*). For the material to begin to crosslink at a given position within the volume, oxygen must be sufficiently depleted locally. The nonlinear response of the material is due to the oxygen inhibition process, which sets a critical dose threshold.

After we exposed the resin from all angles, we observed the full 3D object overcoming inhibition simultaneously and materializing as a whole within the volume (Fig. 1C). This process is quite a departure from conventional AM technologies which build parts serially point-by-point or layer-by-layer. We used highly viscous (up to ~90,000 cP) or solid (thermally gelled) precursor materials to minimize relative motion between the printed object and the precursor. High-viscosity precursors also limited molecular diffusion-induced blurring. After exposure, we removed uncured material by solvent rinsing, sometimes combined with moderate heating to liquefy or reduce the viscosity of the uncured material, to liberate the structure (Fig. 1D). We further cured the 3D part after release using light to enhance material properties (*17*). For material chemistries not inhibited by oxygen, we can obtain dose-response nonlinearity by adding other inhibiting molecules to the resin (*18*, *19*). CAL requires penetration of the curing wavelength through the printing volume, but dye can be added to block other wavelengths and tune component opacity (Fig. 1, F and G).

Using commercially available projection hardware, we demonstrated the capability of our CAL system for fast build times. We completed a centimeter-scale geometry (Fig. 1, C to E) in less than one minute. Using intensities in the range ~0.1–2.0 mW/cm^2, we produced a large range of geometries (Figs. 1 and 2 and fig. S3) with lateral sizes up to ~55 mm, in 30–300 s.

CAL is a physical implementation of the back-projection algorithm used in CT reconstruction, subject to a positivity constraint in the filtered projections (*20*, *21*). Prior work in addressing the volumetric 3D lithography problem used holography and field interference to sculpt 3D energy distributions, with compelling results on sparse or highly symmetric geometries (*9*, *22*). However, the standard digital holography problem is ill-posed due to the dimensionality mismatch between 3D space and 2D projections (*23*). The mathematical framework of CT reconstruction allows for geometric flexibility currently that may be advantageous compared to other techniques. The projection slice theorem governs the relationship between the integral projections and the Fourier transform of the desired target geometry, ensuring that the projections contain the necessary information to construct the object. This relationship underscores the generality of the CAL technique.

We computed the 3D target geometry on a Cartesian voxel basis from the standard stereolithography file format (.stl). This allowed us to use the technique on widely available, 3D-printable, CAD models. As an example we rendered the famous Rodin sculpture, "The Thinker" (Fig. 3A). The z axis was parallel to the axis of rotation of the material volume in Fig. 1B,C. The computation is described for a z-slice of the target geometry $f_T(\mathbf{r}, z)$ which takes the values 1 or 0 representing the desired presence or absence of material. In polar coordinates, the corresponding projection intensities are $g(r, \theta, z)$ in W/cm^2. We used the notation of Tretiak and Metz (*24*) to describe the exponential Radon transform ($T_\alpha[f]$) and its adjoint, the back-projection operator $T_\alpha^*[g]$. We expressed the physically-based forward model that transforms the intensity images into solidified resin as an exponential back-projection operator $T_{-\alpha}^*[g]$ to produce a dose distribution (J/cm^3), followed by a step-function curing operation at the material conversion threshold

$$f(\mathbf{r},z) = I\left\{\frac{\alpha}{\Omega}\left(T_{-\alpha}^*[g](\mathbf{r},z)\right) \geq D_c\right\} = I\left\{\frac{\alpha}{\Omega}\left(\int_{\theta=0}^{2\pi} g\left(\mathbf{r}.\hat{\theta},\theta,z\right)e^{-\alpha \mathbf{r}.\hat{\theta}_\perp}d\theta\right) \geq D_c\right\} \quad (1)$$

where I is an indicator function expressing the threshold, D_c is the critical dose that defines adequate solidification of the material, α is the resin's optical absorption coefficient, and Ω is the rotation rate of the container. The printed geometry $f(\mathbf{r}, z)$ takes the values 0 or 1 to indicate the absence or presence of cured material respectively, and can be directly compared with the target geometry f_T. The coordinate system we used to express the polar unit vectors $\hat{\theta}$ and $\hat{\theta}_\perp$ is shown in Fig. 3B. We defined the intensity projections $g(r, \theta, z)$ on radial lines through the center of the container. Our transformation to projected intensities needs to account for attenuation by the photosensitive material (*17*).

Our desire was to compute projections $g(r, \theta, z)$ such that the printed geometry f closely emulates the desired target geometry f_T. The problem admits an exact solution given by the inverse exponential Radon transform of the 2D dose distribution at each z-slice (*24*, *25*). In other words, back-projecting the analytical inverse of the exponential Radon exactly produced the target geometry. We expressed the inverse through the filtered back-projection formula

$$g_{opt}^{\pm}(r,\theta,z) = \mathcal{F}^{-1}\left\{\hat{W}_\alpha \hat{T}_\alpha\left[f_T\right]\right\} \quad (2)$$

where the $\hat{T}_\alpha$ operator is the Fourier transform of the amplified integral projection of the 2D target geometry

$$\hat{T}_\alpha\left[f_T\right](k,\theta,z) = \int_r\int_t f_T\left(r\hat{\theta}+t\hat{\theta}_\perp\right)e^{\alpha t}e^{-ikr}\,dt\,dr \quad (3)$$

The symbol k is the Fourier conjugate variable to the radius r and $\hat{W}_\alpha(k) = kI_{|k|\geq\alpha}$ is the frequency domain back-projection filter. Spatial frequencies below α are zeroed (*17*, *24*). The ramp filter behaves as a high pass and introduces negative

Downloaded from http://science.sciencemag.org/ on January 31, 2019

excursions to the projection images $g_{opt}^{\pm}(r,\theta,z)$. In the case of negligible attenuation ($\alpha \sim 0$), the filter simplifies to the standard Ram-Lak filter for filtered back-projection (*21*). We also note from the projection slice theorem in the $\alpha \sim 0$ case that the 2D Fourier transform of the "flatland" target geometry for a given z-slice is exactly equal to the 1D Fourier transform of the integral projections along radial samples in the Fourier domain. $\hat{f}(\mathbf{k},z) = \hat{T}_0[f]\left(\mathbf{k}.\hat{\theta},\theta,z\right)$. We illustrated this in Fig. 3D, where the radial samples along the dashed lines are the 1D Fourier transform (in the radius variable) of the integral projections (Fig. 3C).

Although $T_{-\alpha}^{*}\left[g_{opt}^{\pm}\right](\mathbf{r},z)$ produces the target geometry, it will necessarily include negative intensity values. This is a problem in radiation therapy as well, and the dose recipe is typically obtained by iterative optimization while accounting for constraints in the problem formulation (*26*). Because the exact solution in Eq. 3 cannot be implemented by incoherent, temporally multiplexed intensity summation from a projector, the optimal incoherent intensity projections are instead obtained by solving the three-dimensional inverse problem.

$$g_{opt}(r,\theta,z) = \text{argmin} \| f - f_T \|_2 \qquad (4)$$

subject to the constraint $g_{opt} \geq 0$ for intensity-only projections. We used an iterative optimization procedure based on projected gradient descent updates to solve Eq. 4. We found that incorporating the thresholding non-linearity in the problem is critical to obtaining a good correspondence between the dose profile and target geometry (fig. S7).

Optimized projections for "The Thinker" (Fig. 3F) have sharper features than the integral projections shown in panel E above, arising from the filtering operation in the inverse transform. We also show the three-dimensional dose profiles that correspond to their respective projections (Fig. 3, G and H). As expected, the dose distribution resulting from the integral projections (Fig. 3G) is blurred and fails to reproduce sharp geometric features. Further, the dose associated with z-slices containing higher DC content is larger. In contrast, the integrated intensity from the optimized projections (Fig. 3H) matches the target geometry (black line) closely. We used this optimization procedure to generate projection images for a wide variety of geometries that we then printed using CAL (Fig. 2 and fig. S3).

The ability to synthesize custom geometries volumetrically offers a suite of fabrication advantages compared to layer-based AM methods. The elimination of layering resulted in parts with exceptionally smooth surface finishes (Fig. 2, I to L). Additionally, by rapidly fabricating the entire 3D geometry concurrently, CAL required no support structures even when printing re-entrant and overhanging features (e.g., Fig. 2, D to H), or disconnected parts (Fig. 2, D and E). The unique system architecture employed in the CAL fabrication process also offers advantages when the converted material is of low elastic modulus, for example in the ~1–10 kPa regime needed for many soft tissue modeling and bioprinting applications (*27*). We demonstrated this with 3D patterning of a gelatin methacrylate (GelMA) hydrogel material (Fig. 2, I to K, and fig. S3C). Printing this material with a layer-by-layer process would be difficult due to the forces exerted on incomplete structures during the build (*17*).

CAL also widens the field of photopolymers for AM by allowing the use of higher viscosity materials. Layer-based photopolymer printing technologies typically impose a maximum viscosity limit on the pre-polymer mixture to allow the resin to reflow between the printing of subsequent layers. To meet this major design constraint, photopolymer formulations are often blended with reactive diluent monomers (*28*) to reduce the resin viscosity. This process can adversely affect the properties of the resulting solid material. In the CAL process, more viscous materials can be used because flow of the material is not required during printing (*17*). CAL can thus enable printing of materials that are otherwise difficult or slow to 3D-print because of their high viscosity in the precursor form. Example materials include those with high stiffness and thermal resistivity (*29*), along with silicones (*30*).

CAL is well suited for printing material around a complex, pre-existing 3D structure (Fig. 4). The Radon transform possesses a 180° shift symmetry that enables printing of arbitrary geometries onto convex substrates with exposure from the half-space of angles. We synthesized a polymeric handle onto a metal screwdriver shaft (Fig. 4) to demonstrate this ability to synthesize a custom geometry onto an existing mass-manufactured part. We immersed the metal piece in the photopolymer before the rotation during printing. This methodology provides an AM technique analogous to the high-volume injection molding techniques of over-molding and insert molding. We term this AM capability "over-printing," which opens up a wide range of possibilities for multi-process AM. For example, over-printing could be used to encapsulate electronics, improve mechanical properties of orthodontics, or fabricate a customized exterior for an object with a mass-produced skeleton.

Our modeling of light absorption by the rotating resin volume indicates that the illumination time needed for curing can be minimized, for a given projector power, when the resin's absorption coefficient α equals the reciprocal of the printing volume's radius (*31*). This result suggests that CAL is inherently scalable to larger print volumes, with components having diameters ~0.5 m and sub-millimeter features being feasible with the illumination power and resolution of a single commercially available projector. CAL's compatibility with relatively weakly optically absorbing resins, coupled with its low surface roughness, makes it particularly appealing for optical applications. These advantages,

Downloaded from http://science.sciencemag.org/ on January 31, 2019

complemented by the ability to combine materials through over-printing, may motivate the integration of CAL with mass-production and other AM techniques for rapid and cost-effective manufacturing of biomaterials and structures, medical and dental devices, and aerospace applications, to name a few.

REFERENCES AND NOTES

1. E. MacDonald, R. Wicker, Multiprocess 3D printing for increasing component functionality. *Science* **353**, aaf2093 (2016). doi:10.1126/science.aaf2093 Medline
2. X. Wang, S. Xu, S. Zhou, W. Xu, M. Leary, P. Choong, M. Qian, M. Brandt, Y. M. Xie, Topological design and additive manufacturing of porous metals for bone scaffolds and orthopaedic implants: A review. *Biomaterials* **83**, 127–141 (2016). doi:10.1016/j.biomaterials.2016.01.012 Medline
3. A. Bhargav, V. Sanjairaj, V. Rosa, L. W. Feng, J. Fuh Yh, Applications of additive manufacturing in dentistry: A review. *J. Biomed. Mater. Res. B* **106**, 2058–2064 (2018). doi:10.1002/jbm.b.33961 Medline
4. D. T. Nguyen, C. Meyers, T. D. Yee, N. A. Dudukovic, J. F. Destino, C. Zhu, E. B. Duoss, T. F. Baumann, T. Suratwala, J. E. Smay, R. Dylla-Spears, 3D-Printed Transparent Glass. *Adv. Mater.* **29**, 1701181 (2017). doi:10.1002/adma.201701181 Medline
5. H. Gong, B. P. Bickham, A. T. Woolley, G. P. Nordin, Custom 3D printer and resin for 18 μm × 20 μm microfluidic flow channels. *Lab Chip* **17**, 2899–2909 (2017). doi:10.1039/C7LC00644F Medline
6. T. D. Ngo, A. Kashani, G. Imbalzano, K. T. Q. Nguyen, D. Hui, Additive manufacturing (3D printing): A review of materials, methods, applications and challenges. *Compos., Part B Eng.* **143**, 172–196 (2018). doi:10.1016/j.compositesb.2018.02.012
7. A. Gebhardt, J.-S. Hötter, *Additive Manufacturing: 3D Printing for Prototyping and Manufacturing* (Carl Hanser Verlag GmbH & Co. KG, München, 2016); www.hanser-elibrary.com/doi/book/10.3139/9781569905838.
8. E. Sachs, E. Wylonis, S. Allen, M. Cima, H. Guo, Production of Injection Molding Tooling With Conformal Cooling Channels Using the Three Dimensional Printing Process. *Polym. Eng. Sci.* **40**, 1232–1247 (2000). doi:10.1002/pen.11251
9. M. Shusteff, A. E. M. Browar, B. E. Kelly, J. Henriksson, T. H. Weisgraber, R. M. Panas, N. X. Fang, C. M. Spadaccini, One-step volumetric additive manufacturing of complex polymer structures. *Sci. Adv.* **3**, eaao5496 (2017). doi:10.1126/sciadv.aao5496 Medline
10. C. W. Hull, Apparatus for production of three-dimensional objects by stereolithography, U.S. Patent 4,575,330 (1986).
11. J. R. Tumbleston, D. Shirvanyants, N. Ermoshkin, R. Janusziewicz, A. R. Johnson, D. Kelly, K. Chen, R. Pinschmidt, J. P. Rolland, A. Ermoshkin, E. T. Samulski, J. M. DeSimone, Additive manufacturing. Continuous liquid interface production of 3D objects. *Science* **347**, 1349–1352 (2015). doi:10.1126/science.aaa2397 Medline
12. P. F. Jacobs, *Rapid Prototyping & Manufacturing: Fundamentals of StereoLithography* (Society of Manufacturing Engineers, Dearborn, MI, 1st edition, 1992).
13. G. N. Hounsfield, Method and apparatus for measuring x- or γ-radiation absorption or transmission at plural angles and analyzing the data, U.S. Patent 3,778,614 (1973).
14. J. Kastner, C. Heinzl, in *Integrated Imaging and Vision Techniques for Industrial Inspection* (Springer, London, 2015), *Advances in Computer Vision and Pattern Recognition*, pp. 227–250.
15. T. Bortfeld, J. Bürkelbach, R. Boesecke, W. Schlegel, Methods of image reconstruction from projections applied to conformation radiotherapy. *Phys. Med. Biol.* **35**, 1423–1434 (1990). doi:10.1088/0031-9155/35/10/007 Medline
16. A. K. O'Brien, C. N. Bowman, Impact of oxygen on photopolymerization kinetics and polymer structure. *Macromolecules* **39**, 2501–2506 (2006). doi:10.1021/ma051863l
17. Materials and methods are available as supplementary materials.
18. S. S. Cutié, D. E. Henton, C. Powell, R. E. Reim, P. B. Smith, T. L. Staples, The effects of MEHQ on the polymerization of acrylic acid in the preparation of superabsorbent gels. *J. Appl. Polym. Sci.* **64**, 577–589 (1997). doi:10.1002/(SICI)1097-4628(19970418)64:3<577:AID-APP14>3.0.CO;2-V
19. M. P. de Beer, H. L. van der Laan, M. A. Cole, R. J. Whelan, M. A. Burns, T. F. Scott, Rapid, continuous additive manufacturing by volumetric polymerization inhibition patterning. *Sci. Adv.* **5**, eaau8723 (2019). doi:10.1126/sciadv.aau8723
20. A. C. Kak, M. Slaney, *Principles of Computerized Tomographic Imaging* (Society of Industrial and Applied Mathematics, 2001).
21. G. N. Ramachandran, A. V. Lakshminarayanan, Three-dimensional reconstruction from radiographs and electron micrographs: Application of convolutions instead of Fourier transforms. *Proc. Natl. Acad. Sci. U.S.A.* **68**, 2236–2240 (1971). doi:10.1073/pnas.68.9.2236 Medline
22. J. Zhang, N. Pégard, J. Zhong, H. Adesnik, L. Waller, 3D computer-generated holography by non-convex optimization. *Optica* **4**, 1306–1313 (2017). doi:10.1364/OPTICA.4.001306
23. R. Piestun, B. Spektor, J. Shamir, Wave fields in three dimensions: Analysis and Synthesis. *J. Opt. Soc. Am. A Opt. Image Sci. Vis.* **13**, 1837–1848 (1996). doi:10.1364/JOSAA.13.001837
24. O. Tretiak, C. Metz, The Exponential Radon Transform. *SIAM J. Appl. Math.* **39**, 341–354 (1980). doi:10.1137/0139029
25. F. Natterer, Inversion of the attenuated Radon transform. *Inverse Probl.* **17**, 113–119 (2001). doi:10.1088/0266-5611/17/1/309
26. M. Ehrgott, Ç. Güler, H. W. Hamacher, L. Shao, Mathematical optimization in intensity modulated radiation therapy. *Ann. Oper. Res.* **175**, 309–365 (2010). doi:10.1007/s10479-009-0659-4
27. S. V. Murphy, A. Atala, 3D bioprinting of tissues and organs. *Nat. Biotechnol.* **32**, 773–785 (2014). doi:10.1038/nbt.2958 Medline
28. J. W. Lee, P. X. Lan, B. Kim, G. Lim, D.-W. Cho, 3D scaffold fabrication with PPF/DEF using micro-stereolithography. *Microelectron. Eng.* **84**, 1702–1705 (2007). doi:10.1016/j.mee.2007.01.267
29. M. Hegde, V. Meenakshisundaram, N. Chartrain, S. Sekhar, D. Tafti, C. B. Williams, T. E. Long, 3D Printing All-Aromatic Polyimides using Mask-Projection Stereolithography: Processing the Nonprocessable. *Adv. Mater.* **29**, 1701240 (2017). doi:10.1002/adma.201701240 Medline
30. A. S. Wu, W. Small Iv, T. M. Bryson, E. Cheng, T. R. Metz, S. E. Schulze, E. B. Duoss, T. S. Wilson, 3D Printed Silicones with Shape Memory. *Sci. Rep.* **7**, 4664 (2017). doi:10.1038/s41598-017-04663-z Medline
31. Printing rate modeling can be found in the supplementary materials, sections S18–S21.
32. K. S. Lim, B. S. Schon, N. V. Mekhileri, G. C. J. Brown, C. M. Chia, S. Prabakar, G. J. Hooper, T. B. F. Woodfield, New Visible-Light Photoinitiating System for Improved Print Fidelity in Gelatin-Based Bioinks. *ACS Biomater. Sci. Eng.* **2**, 1752–1762 (2016). doi:10.1021/acsbiomaterials.6b00149
33. B. Kelly, I. Bhattacharya, M. Shusteff, H. Taylor, C. Spadaccini, Computed Axial Lithography (CAL) for Rapid Volumetric 3D Additive Manufacturing, presented at *Solid Freeform Fabrication* (2017); available at: http://sffsymposium.engr.utexas.edu/sites/default/files/2017/Manuscripts/ComputedAxialLithographyforRapidVolumetric3D.pdf [accessed Aug. 16, 2018].
34. B. Kelly *et al.*, Computed Axial Lithography (CAL): Toward Single Step 3D Printing of Arbitrary Geometries. *arXiv:1705.05893 [cs]* (2017) (available at http://arxiv.org/abs/1705.05893).
35. D. M. Ebenstein, Nano-JKR force curve method overcomes challenges of surface detection and adhesion for nanoindentation of a compliant polymer in air and water. *J. Mater. Res.* **26**, 1026–1035 (2011). doi:10.1557/jmr.2011.42
36. Carbon, Inc., Technical Data Sheet for Flexible Polyurethane (FPU) 3D Printer Material; available at www.carbon3d.com/materials/fpu-flexible-polyurethane/ [accessed Jan. 16, 2019].
37. N. Otsu, A Threshold Selection Method from Gray-Level Histograms. *IEEE Trans. Syst. Man Cybern.* **9**, 62–66 (1979). doi:10.1109/TSMC.1979.4310076
38. P. Kuchment, Generalized Transforms of Radon Type and their Application, in *The Radon Transform, Inverse Problems, and Tomography*, vol. 63 of *Proceedings of Symposia in Applied Mathematics*, eds. G. Ólafsson, E. Quinto, American Mathematical Society (2006). DOI: 10.1090/psapm/063/2208237
39. X. Zhang, X. N. Jiang, C. Sun, Micro-stereolithography of polymeric and ceramic microstructures. *Sens. Actuators A* **77**, 149–156 (1999). doi:10.1016/S0924-4247(99)00189-2
40. C. Sun, N. Fang, D. M. Wu, X. Zhang, Projection micro-stereolithography using digital micro-mirror dynamic mask. *Sens. Actuators A* **121**, 113–120 (2005). doi:10.1016/j.sna.2004.12.011

Downloaded from http://science.sciencemag.org/ on January 31, 2019

41. H. M. Laun, M. Rady, O. Hassager, Analytical solutions for squeeze flow with partial wall slip. *J. Non-Newt. Fluid Mech.* **81**, 1–15 (1999). doi:10.1016/S0377-0257(98)00083-4
42. X. Zheng, H. Lee, T. H. Weisgraber, M. Shusteff, J. DeOtte, E. B. Duoss, J. D. Kuntz, M. M. Biener, Q. Ge, J. A. Jackson, S. O. Kucheyev, N. X. Fang, C. M. Spadaccini, Ultralight, ultrastiff mechanical metamaterials. *Science* **344**, 1373–1377 (2014). doi:10.1126/science.1252291 Medline
43. Carbon, Inc., Safety Data Sheet for UMA90 resin; available at: www.tth.com/wp-content/uploads/103367-UMA-90-US-SDS.pdf [accessed Aug. 14, 2018].
44. Carbon, Inc., Technical Data Sheet for UMA90 resin; available at: https://s3.amazonaws.com/carbon-static-assets/downloads/resin_data_sheets/UMA90_TDS.pdf [accessed Aug. 15, 2018].
45. S. Yuan, F. Liu, J. He, Preparation and Characterization of Low Polymerization Shrinkage and Bis-GMA-Free Dental Resin System. *Adv. Polym. Technol.* **34**, 21503 (2015). doi:10.1002/adv.21503
46. H. P. Greenspan, L. N. Howard, On a time-dependent motion of a rotating fluid. *J. Fluid Mech.* **17**, 385–404 (1963). doi:10.1017/S0022112063001415
47. W. B. Watkins, R. G. Hussey, Spin-up from rest in a cylinder. *Phys. Fluids* **20**, 1596–1604 (1977). doi:10.1063/1.861781
48. J. Sharpe, U. Ahlgren, P. Perry, B. Hill, A. Ross, J. Hecksher-Sørensen, R. Baldock, D. Davidson, Optical projection tomography as a tool for 3D microscopy and gene expression studies. *Science* **296**, 541–545 (2002). doi:10.1126/science.1068206 Medline
49. H. Zollinger, *Color Chemistry: Syntheses, Properties, and Applications of Organic Dyes and Pigments* (John Wiley & Sons, 2003).
50. Luminus Devices, Inc, Luminus CBT-39 LED product datasheet; available at https://download.luminus.com/datasheets/Luminus_CBT-39-UV_Datasheet.pdf [accessed Jan. 16, 2019].

ACKNOWLEDGMENTS

We thank R. McLeod, R. Ng, J. Oakdale, R. Panas, L. Waller, and J. Zhang for helpful discussions. We gratefully acknowledge assistance with nanoindentation from S. E. Arevalo, assistance with tensile testing from A. Jordan, assistance with roughness measurements from I. Ladner, and the gift of a projector module from R. Weitekamp. **Funding:** This work was supported by U.C. Berkeley faculty start-up funds (to H.T.) and by Lawrence Livermore National Laboratory Laboratory-Directed Research and Development funding 14-SI-004 (to C.S.) and 17-ERD-116 (to M.S.). The work was performed under the auspices of the U.S. Department of Energy by Lawrence Livermore National Laboratory under Contract DE-AC52-07NA27344 (LLNL-JRNL-755660). **Author contributions:** H.T., M.S., and C.S. designed the research and provided the overall direction; B.K., H.H., H.T., and M.S. designed experiments; B.K. and H.H. conducted experiments; I.B. developed the projection computation algorithm; H.T. and I.B. built the process models; all authors contributed to analysis and to writing and refining the manuscript. **Competing interests:** The authors are inventors on a U.S. patent application related to this work (15/593,947). All authors declare that they have no other competing interests. **Data and materials availability:** All data are available in the manuscript or the supplementary materials. Algorithm pseudo-code is available in the supplementary materials (section S12).

SUPPLEMENTARY MATERIALS

www.sciencemag.org/cgi/content/full/science.aau7114/DC1
Materials and Methods
Supplementary Text
Figs. S1 to S20
Tables S1 to S3
References (*32*–*50*)
Movies S1 to S5

17 August 2018; resubmitted 5 December 2018
Accepted 18 January 2019
Published online 31 January 2019
10.1126/science.aau7114

Downloaded from http://science.sciencemag.org/ on January 31, 2019

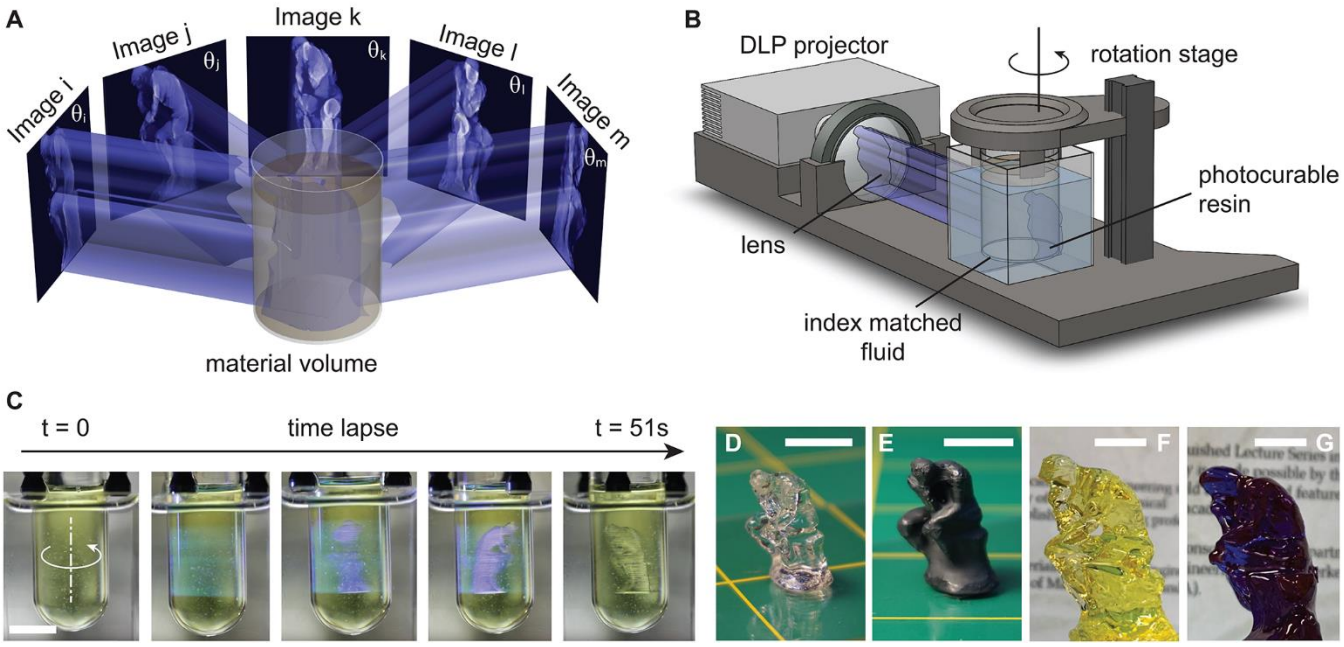

Fig. 1. CAL volumetric fabrication. (A) Underlying concept: patterned illumination from many directions delivers a computed 3D exposure dose to a photoresponsive material. (B) Schematic of CAL system used in this work. (C) Sequential view of the build volume during a CAL print. A 3D geometry is formed in the material in less than a minute. (D) The 3D part shown in (C) after rinsing away uncured material. (E) The part from (D) painted for clarity. (F) A larger (40 mm-tall) version of the same geometry. (G) Opaque version of the geometry in (F), using crystal violet dye in the resin. Scale bars: 10 mm.

Downloaded from http://science.sciencemag.org/ on January 31, 2019

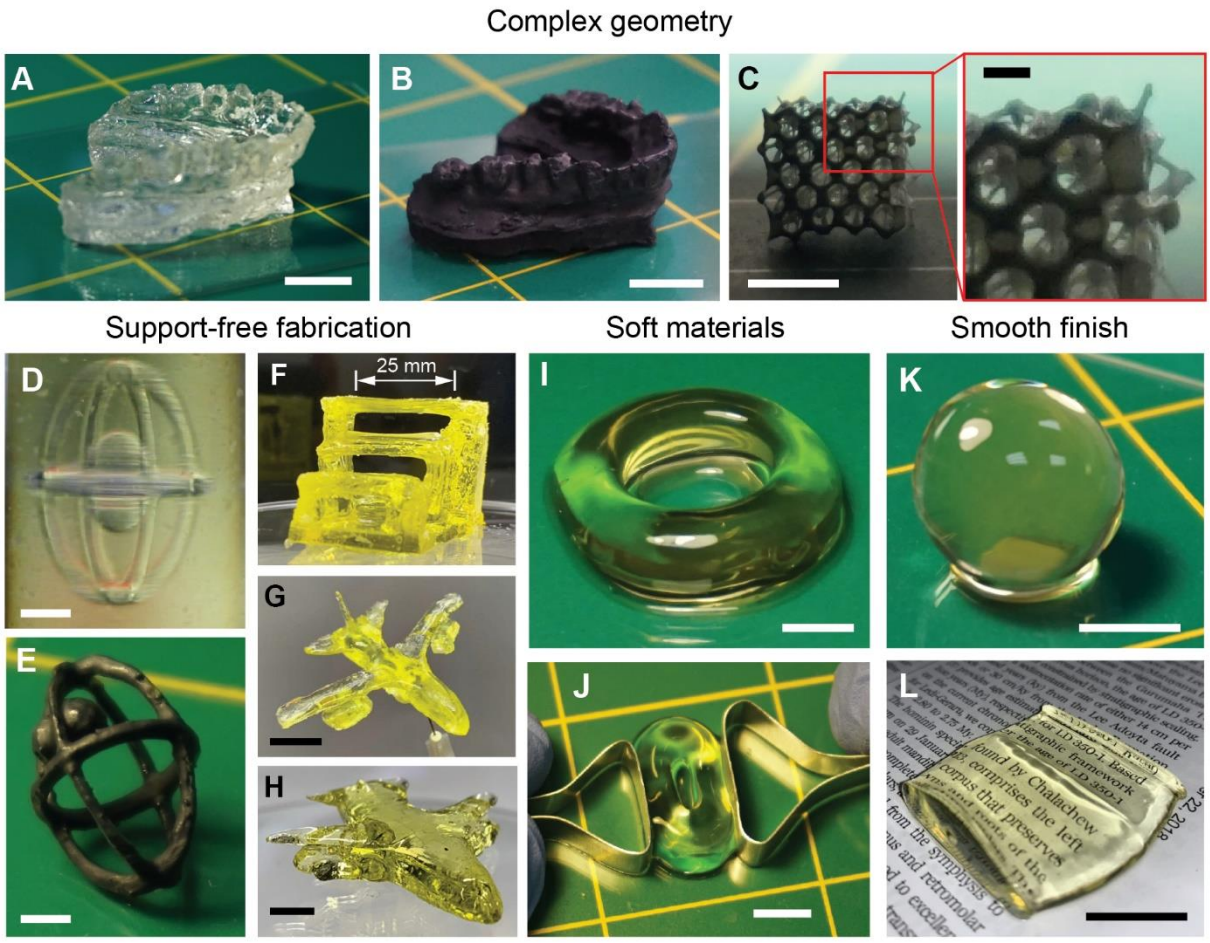

Fig. 2. Parts fabricated by CAL. (A) A highly complex geometry (dental model). (B) Same part as in (A) painted for clarity. (C) Complex lattice geometry with fine features as small as 0.3 mm and internal voids. (D) "Ball-in-a-cage" geometry: an example of a disconnected part printed without solid support structures. Part is suspended in uncured material. (E) Part in (D) removed from uncured material and painted for clarity. (F) Bridges with unsupported spans up to 25 mm. (G and H) Airplanes with sharp wing tips and overhanging wings. (I and J) Donut printed in highly deformable GelMA hydrogel, showing a smooth, layer-less surface finish. (K) Smooth sphere without layering artifacts. (L) Component with smooth planar and convex curved regions. Scale bars: (A, B, L) 10 mm; (C, G to K): 5 mm (C inset: 1 mm); (D, E): 2 mm.

Downloaded from http://science.sciencemag.org/ on January 31, 2019

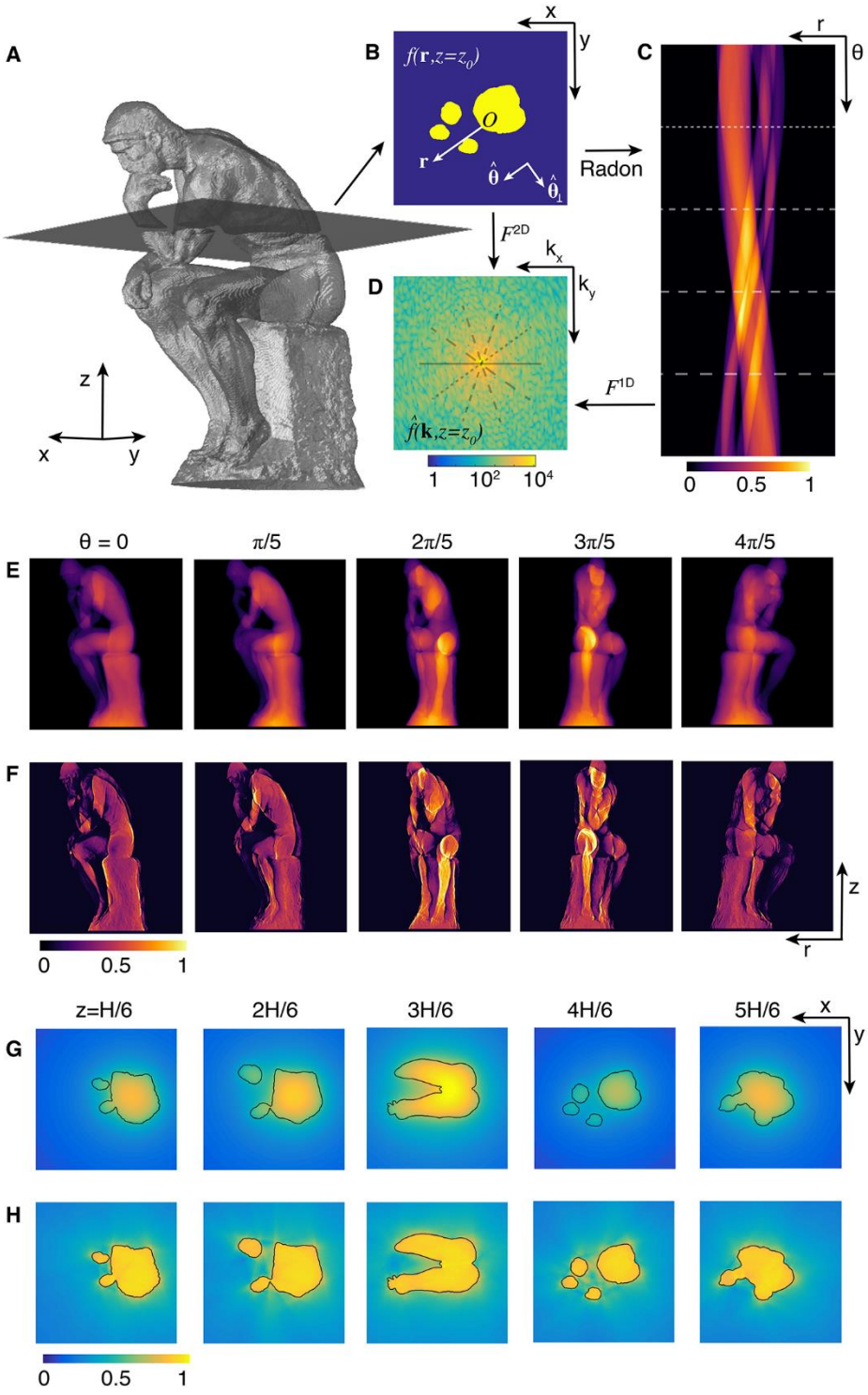

Fig. 3. Projection computation. (A) 3D target object; (B) *z* cross-section; (C) Radon transform; (D) 2D Fourier transform; (E) Integral projections at example angles; (F) Optimized projections; (G) Cumulative dose from back-projection of integral projection; (H) Optimized cumulative dose.

Downloaded from http://science.sciencemag.org/ on January 31, 2019

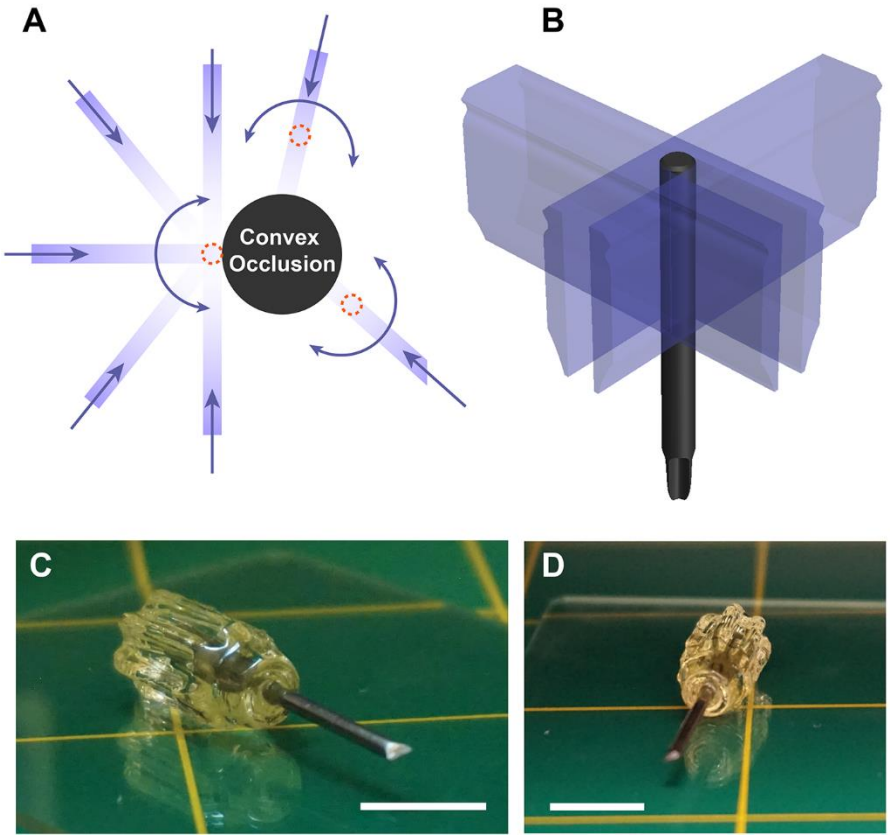

Fig. 4. CAL enables over-printing of 3D geometries around pre-existing solid components. A convex occlusion allows access from the half space (**A** and **B**), permitting delivery of the projections needed to cure custom geometries around the occlusion. (**C** and **D**) Example of a screwdriver handle printed using CAL to encase a metallic shaft (scale-bars: 10 mm).

Downloaded from http://science.sciencemag.org/ on January 31, 2019

Science

Volumetric additive manufacturing via tomographic reconstruction

Brett E. Kelly, Indrasen Bhattacharya, Hossein Heidari, Maxim Shusteff, Christopher M. Spadaccini and Hayden K. Taylor

published online January 31, 2019

ARTICLE TOOLS http://science.sciencemag.org/content/early/2019/01/30/science.aau7114

SUPPLEMENTARY MATERIALS http://science.sciencemag.org/content/suppl/2019/01/30/science.aau7114.DC1

REFERENCES This article cites 40 articles, 10 of which you can access for free
http://science.sciencemag.org/content/early/2019/01/30/science.aau7114#BIBL

PERMISSIONS http://www.sciencemag.org/help/reprints-and-permissions

Use of this article is subject to the Terms of Service

Science (print ISSN 0036-8075; online ISSN 1095-9203) is published by the American Association for the Advancement of Science, 1200 New York Avenue NW, Washington, DC 20005. 2017 © The Authors, some rights reserved; exclusive licensee American Association for the Advancement of Science. No claim to original U.S. Government Works. The title *Science* is a registered trademark of AAAS.

Downloaded from http://science.sciencemag.org/ on January 31, 2019